Article

Understanding Dioxygen Activation in the Fe(III)-Promoted Oxidative Dehydrogenation of Amines: A Computational Study

Ricardo D. Páez-López [1], Miguel Á. Gómez-Soto [2], Héctor F. Cortés-Hernández [3], Alejandro Solano-Peralta [1], Miguel Castro [2], Peter M. H. Kroneck [4] and Martha E. Sosa-Torres [1,*]

[1] Departamento de Química Inorgánica y Nuclear, Facultad de Química, Universidad Nacional Autónoma de México, Ciudad Universitaria, Mexico City 04510, Mexico; richie_daniels@comunidad.unam.mx (R.D.P.-L.); alejandro.solano@quimica.unam.mx (A.S.-P.)

[2] Departamento de Física y Química Teórica, Facultad de Química, Universidad Nacional Autónoma de México, Ciudad Universitaria, Mexico City 04510, Mexico; gsgomezsoto@gmail.com (M.Á.G.-S.); miguel.castro.m@gmail.com (M.C.)

[3] GIFAMol, Grupo de Investigación en Fisicoquímica Aplicada y Modelamiento Molecular, Escuela de Tecnología Química, Universidad Tecnológica de Pereira, Pereira 660003, Colombia; hfcortes@utp.edu.co

[4] Department of Biology, University of Konstanz, D-78457 Konstanz, Germany; peter.kroneck@uni-konstanz.de

* Correspondence: mest@unam.mx; Tel.: +52-55-5622-3808

Abstract: Hydrogenation and dehydrogenation reactions are fundamental in chemistry and essential for all living organisms. We employ density functional theory (DFT) to understand the reaction mechanism of the oxidative dehydrogenation (ODH) of the pyridyl-amine complex $[Fe^{III}L^3]^{3+}$ (L^3, 1,9-bis(2'-pyridyl)-5-[(ethoxy-2''-pyridyl)methyl]-2,5,8-triazanonane) to the mono-imine complex $[Fe^{II}L^4]^{2+}$ (L^4, 1,9-bis(2'-pyridyl)-5-[(ethoxy-2''-pyridyl)methyl]-2,5,8-triazanon-1-ene) in the presence of dioxygen. The nitrogen radical $[Fe^{II}L^3_{N8\bullet}]^{2+}$, formed by deprotonation of $[Fe^{III}L^3]^{3+}$, plays a crucial role in the reaction mechanism derived from kinetic studies. O_2 acts as an oxidant and is converted to H_2O. Experiments with the deuterated ligand L^3 reveal a primary C-H kinetic isotope effect, $k^{CH}/k^{CD} = 2.30$, suggesting C-H bond cleavage as the rate-determining step. The DFT calculations show that (i) $^3O_2$ abstracts a hydrogen atom from the α-pyridine aliphatic C-H moiety, introducing a double bond regio-selectively at the C_7N_8 position, via the hydrogen atom transfer (HAT) mechanism, (ii) O_2 does not coordinate to the iron center to generate a high-valent Fe oxo species observed in enzymes and biomimetic complexes, and (iii) the experimental activation parameters ($\Delta H^{\neq} = 20.38$ kcal mol^{-1}, $\Delta S^{\neq} = -0.018$ kcal mol^{-1} K^{-1}) fall within in the range of values reported for HAT reactions and align well with the computational results for the activated complex $[Fe^{II}L^3_{N8\bullet}]^{2+}\cdots^3O_2$.

Keywords: oxidative dehydrogenation; hydrogen atom transfer; density functional theory; nitrogen radical; dioxygen activation; regio-selective C-H cleavage

1. Introduction

Oxidative dehydrogenation (ODH) reactions of alcohols and amines play vital roles in all living organisms. Through evolutionary refinement, nature has evolved enzymes that host transition metals, e.g., iron (Fe), copper (Cu), and zinc (Zn), as well as redox non-innocent ligands at the active site, to oxidize these substrates [1–4]. Current research focuses on creating affordable biomimetic metal catalysts to functionalize C-H bonds. This task poses a considerable challenge for synthetic chemists, particularly when it comes to controlling regio- and site selectivity during the synthesis and transformation of molecules [5]. Dioxygen (O_2), or hydrogen peroxide (H_2O_2) typically serve as oxidizing

agents to perform reactions under mild conditions [6,7]. For example, the Fe(II) complex [Fe(H)(BH$_4$)(CO)(HN{CH$_2$CH$_2$P(iPr)$_2$}$_2$)] catalyzes the ODH of secondary alcohols to ketones, with good yields in the presence of O$_2$. A base is necessary to facilitate ligand activation, forming a Fe(II)-amido intermediate that can abstract hydrogen atoms from C-H bonds in alcohols through a concerted outer-sphere m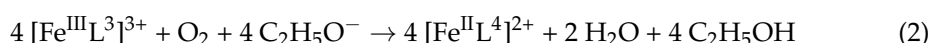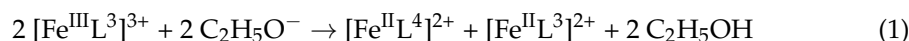echanism [8]. Similarly, Fe(II) complexes with NNN donor azo-aromatic pincer ligands catalyze the oxidation of benzylic alcohols to carbonyls. In this instance, the ligand undergoes a one-electron reduction initiated by ethoxide N-H deprotonation. This forms an azo-anion radical intermediate, which then reacts by abstracting an H atom from the α-carbon of coordinated alcohol [9] through hydrogen atom transfer (HAT) [10].

We are interested in gaining a deeper understanding of transition metal-promoted ODH reactions in the presence of dioxygen. Specifically, we aim to understand the conversion of the paramagnetic complex [Fe^{III}L^3]$^{3+}$ (**1**) (L^3, 1,9-bis(2′-pyridyl)-5-[(ethoxy-2″-pyridyl)methyl]-2,5,8-triazanonane) to the diamagnetic complex [Fe^{II}L^4]$^{2+}$ (**2**) (L^4, 1,9-bis(2′-pyridyl)-5-[(ethoxy-2″-pyridyl)methyl]-2,5,8-triazanon-1-ene) characterized by multinuclear NMR spectroscopy and X-ray crystallography (CCDC ref 286407) (Figure 1) [11–13].
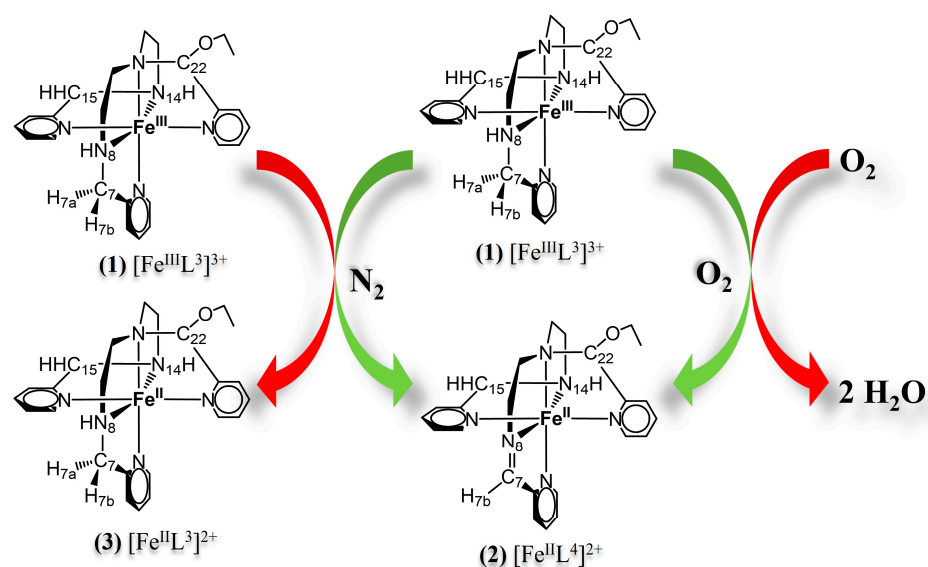
Figure 1. Oxidative dehydrogenation of pyridyl–amine Fe(III) complex (**1**), [Fe^{III}L^3]$^{3+}$, to mono–imine Fe(II) complex (**2**), [Fe^{II}L^4]$^{2+}$, and (**3**), [Fe^{II}L^3]$^{2+}$ in anoxic (N$_2$, no external oxidant) and oxic (oxidant O$_2$) conditions.

The Fe(III) complex (**1**) is unique due to its ODH reactivity in anoxic (Equation (1)) and oxic (Equation (2)) conditions (Figure 1) [12,13].

$$2\,[Fe^{III}L^3]^{3+} + 2\,C_2H_5O^- \rightarrow [Fe^{II}L^4]^{2+} + [Fe^{II}L^3]^{2+} + 2\,C_2H_5OH \tag{1}$$

$$4\,[Fe^{III}L^3]^{3+} + O_2 + 4\,C_2H_5O^- \rightarrow 4\,[Fe^{II}L^4]^{2+} + 2\,H_2O + 4\,C_2H_5OH \tag{2}$$

Notably, only one double bond is introduced at position C$_7$N$_8$ of ligand L^3, in contrast to the reports for numerous polydentate amine complexes [14]. Conjugation of the C=N double bond to the pyridine ring stabilizes the Fe^{II} oxidation state via its π-acceptor capability, consistent with the high redox potential reported [11,12]. The ODH reaction proceeds faster with O$_2$ and does not show the N-H kinetic isotope effect (KIE) observed in N$_2$ (k^{NH}/k^{ND} = 1.73) [12]. Both reactions, performed in dry ethanol, require a base, C$_2$H$_5$O$^-$. Deprotonation of complex (**1**) leads to the nitrogen radical [Fe^{II}L^3$_{N8•}$]$^{2+}$ (**2a**) which has been suggested to reduce O$_2$ via four consecutive outer-sphere single electron transfer steps to H$_2$O [13]. With the deuterated pyridyl-amine ligand L^3-D, we observed a

C-H KIE k^{CH}/k^{CD} with a value of 2.30 for the rate-determining step of the ODH reaction. ^{2}H NMR analysis of the deuterated mono-imine product $[Fe^{II}L^4\text{-}D]^{2+}$ (**2**) indicates regio-selective C-H cleavage by O_2 at the C_7N_8 position through the hydrogen atom transfer (HAT) mechanism, generating the $HO_2{}^\bullet$ radical [15].

With the results of these kinetic studies in hand, we have proposed that nitrogen $N_{8\bullet}$ in radical $[Fe^{II}L^3{}_{N8\bullet}]^{2+}$ (**2a**) transfers charge to the Fe(II) center, lowering the dissociation energy of the $C_7\text{-}H_a$ bond. In the transition state (TS) the iron complex exhibits a biradical character and facilitates hydrogen atom transfer (HAT) to $^3O_2$ in the rate-determining step (Figure 2), consistent with the observed C-H KIE and the experimentally determined third-order rate law in Equation (3). The final product of the ODH reaction, the diamagnetic mono-imine $[Fe^{II}L^4]^{2+}$ (**2**), has already been characterized by spectroscopic techniques and X-ray crystallography using tetraphenyl borate as a counter anion [12,13,15].

$$-\frac{d\left[Fe^{III}L^3\right]^{3+}}{dt} = k_{ODH}\left[\left[Fe^{III}L^3\right]^{3+}\right][O_2]\left[C_2H_5O^-\right] \qquad (3)$$
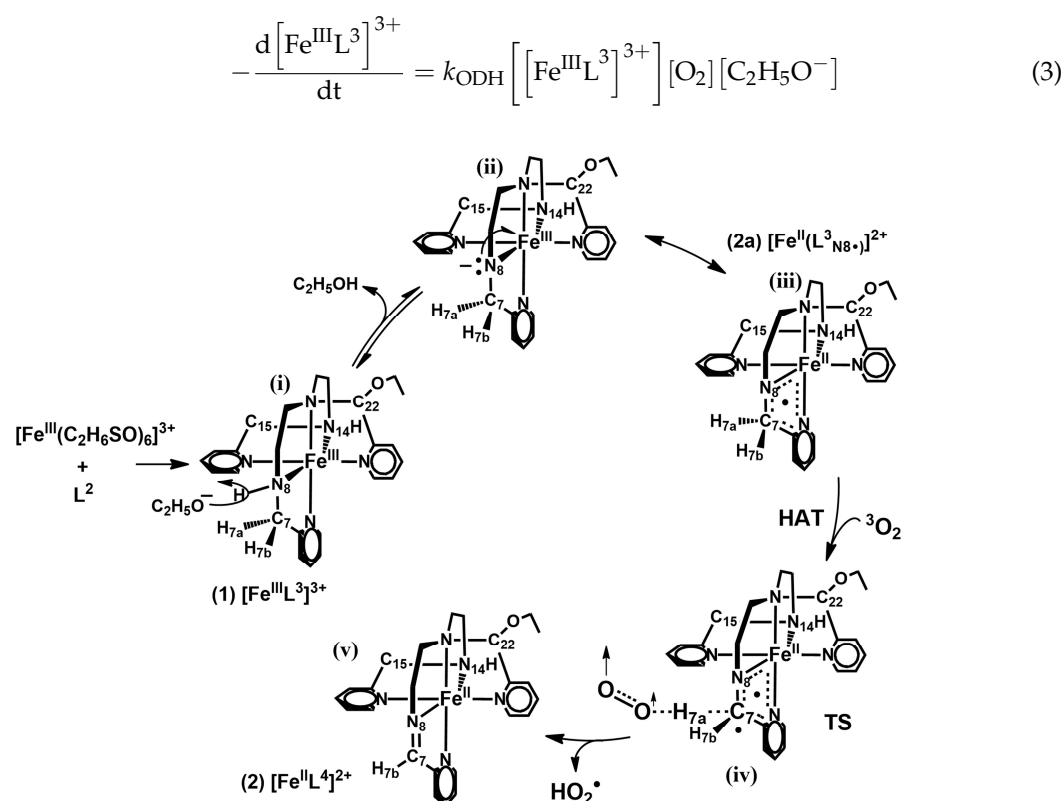
Figure 2. A mechanistic proposal for the oxidative dehydrogenation of pyridyl–amine Fe(III) complex $[Fe^{III}L^3]^{3+}$ (**1**) in the presence of dioxygen. (i) $[Fe^{III}L^3]^{3+}$ (**1**) is attacked by $C_2H_5O^-$ producing the amido compound (ii), described as the delocalized "resonance" nitrogen radical (**2a**) (iii) which then is attacked by O_2 via HAT in the rate limiting step, k_2 (Equation (A2)), to form the transition state (iv). Note that there is a regioselective hydrogen abstraction (H_{7a}) to produce the final compounds (**2**) and $HO_2{}^\bullet$.

The current work presents a computational study to validate the proposed reaction mechanism (Figure 2). We aim to understand the pathway of the ODH reaction of Fe(III) complex (**1**) with external oxidant O_2 and the crucial role of nitrogen radical (**2a**). We are also interested in identifying the preferred site for the O_2 attack leading to regio-selective dehydrogenation and imine formation. In this study, we describe various calculated structures, geometries, spin states, and conceptual DFT analyses to determine the most favorable configuration for hydrogen atom transfer.

2. Results

2.1. Ligands and Iron Complexes

The pyridyl-amine Fe(III) complex (**1**) is formed by mixing solutions of ligand L^2-H/L^2-D (L^2, 1-[3-aza-4-(2-pyridyl)-butyl]-2-(2-pyridyl)-3-[(2-pyridyl)-methyl] imidazolidine/deuterated analog) and dimethyl sulfoxide complex $[Fe^{III}(C_2H_6OS)_6](NO_3)_3$ in ethanol. The imidazolidine ligand L^2 undergoes a ring-opening reaction to form the low-spin complex $[Fe^{III}L^3]^{3+}$ (**1**) (M = 2; λ_{max} 366 nm/3390 M^{-1} cm^{-1}, 582 nm/528 M^{-1} cm^{-1}) followed by its deprotonation to the nitrogen radical (**2a**) and the ODH reaction to the mono-imine complex $[Fe^{II}L^4]^{2+}$ (**2**) (M = 10; λ_{max} 398 nm/8036 M^{-1} cm^{-1}, 573 nm/6984 M^{-1} cm^{-1}) [12,13].

Synthesis of L^2-D leads to a 1:1-mixture of the imidazolidine isomers L^2-C_7DHC_{15}HH and L^2-C_7HHC_{15}DH, and its reaction with $[Fe^{III}(C_2H_6OS)_6](NO_3)_3$ results in two Fe(III) complexes (**1**) mono-deuterated at either carbon C_7 or carbon C_{15} [15]. As mentioned, only one double bond is introduced at position C_7N_8 of the hexadentate ligand L^3 to produce L^4. Furthermore, there is no evidence for the in situ generation of singlet oxygen, $^1O_2$ (M = 1), by EPR spectroscopy employing the trapping agent 2,2,6,6-tetramethyl-4-piperidinol (TEMP) [16], in contrast to reports on the dehydrogenation of Ir(III) amino acid complexes under blue light [17], or the in situ production of $^1O_2$ by dioxygen activation on iron phosphide for advanced oxidation processes [18]. Therefore, the primary focus of the computational studies will be on the C_7N_8 region of Fe(III) complex (**1**) and its reactivity with triplet oxygen, $^3O_2$ (M = 3).

The optimized structures of Fe(III) complex (**1**) (Figure A1) and nitrogen radical (**2a**) (Figure 3) were calculated using the DFT-PBE-Def2SVP method, as implemented in the Gaussian 09 program [19]. The X-ray coordinates of $[Fe^{II}L^4][C_6H_5)_4]_2$ (CCDC-286407) were chosen for the initial input geometry.
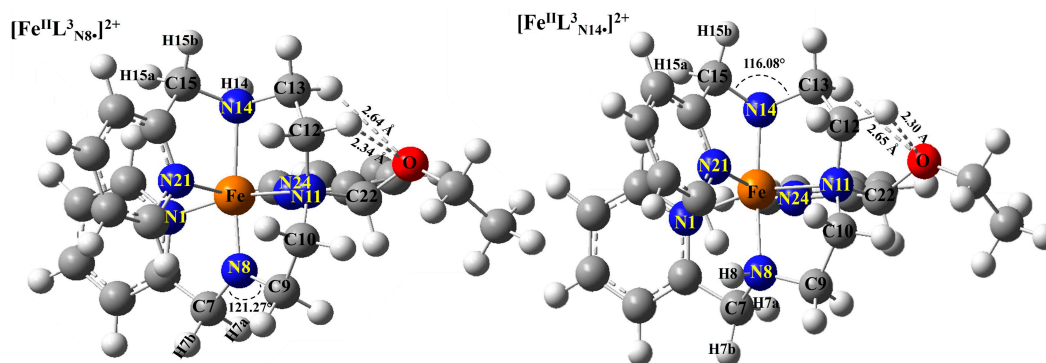
Figure 3. Optimized structures of nitrogen radicals (**2a**): $[Fe^{II}L^3_{N8\bullet}]^{2+}$ and $[Fe^{II}L^3_{N14\bullet}]^{2+}$ calculated using the X–ray coordinates of $[Fe^{II}L^4][C_6H_5)_4]_2$ (CCDC–286407); Fe orange, H white, C grey, N blue, O red.

2.2. Nitrogen Radical $[Fe^{II}L^3_{N8\bullet}]^{2+}$ and Site for O_2 Attack

First, the total energies for the reactants and products of the ODH reaction (Figure 2) have been calculated. For both the starting Fe(III) complex (**1**) and Fe(II) radical (**2a**), a doublet ground state (M = 2) was found to have the minimum energy, and a singlet ground state (M = 1), for the mono-imine Fe(II) complex (**2**) (Table 1).

Table 1. Calculated energies (kcal mol^{-1}) for [Fe^{III}L^3]$^{3+}$ (**1**), C$_2$H$_5$O$^-$, [Fe^{II}L^3$_{N8\bullet}$]$^{2+}$ (**2a**), C$_2$H$_5$OH, O$_2$, {[Fe^{II}L^3$_{N8\bullet\,C7\bullet}$]$^{2+}$---H$_{7a}$---^{3}O$_2$} (**TS**), [Fe^{II}L^4]$^{2+}$ (**2**), and HO$_2$$^\bullet$; M, multiplicity; EE, electronic energy; ZPE, zero–point energy; TEC, thermal enthalpy correction; TS, transition state.

Species	M	EE + ZPE (kcal mol^{-1})	EE + TEC (kcal mol^{-1})
[Fe^{III}L^3]$^{3+}$, (**1**)	2	−1,629,611.901	−1,629,593.709
	4	−1,629,599.929	−1,629,581.205
	6	−1,629,597.183	−1,629,577.986
C$_2$H$_5$O$^-$	1	−96,657.889	−96,654.857
[Fe^{II}L^3$_{N8\bullet}$]$^{2+}$ (**2a**)	2	−1,629,517.246	−1,629,499.171
	4	−1,629,500.632	−1,629,481.836
	6	−1,629,495.890	−1,629,476.821
C$_2$H$_5$OH	1	−97,041.209	−97,037.904
O$_2$	3	−94,164.405	−94,162.330
{[Fe^{II}L^3$_{N8\bullet\,C7\bullet}$]$^{2+}$--- H$_{7a}$---^{3}O$_2$} (**TS**)	4	−1,723,662.304	−1,723,642.314
[Fe^{II}L^4]$^{2+}$ (**2**)	1	−1,629,159.347	−1,629,141.605
	3	−1,629,138.195	−1,629,119.575
	5	−1,629,138.422	−1,629,119.446
HO$_2$$^\bullet$	2	−94,518.050	−94,515.661

According to the DFT calculations, complex [Fe^{III}L^3]$^{3+}$ (**1**) undergoes deprotonation of the N$_8$-H bond with the base C$_2$H$_5$O$^-$, resulting in the formation of the radical [Fe^{II}L^3$_{N8\bullet}$]$^{2+}$ (**2a**), with an energy = −1,629,517.246 kcal mol^{-1}. On the other hand, deprotonation of N$_{14}$-H leads to the formation of radical [Fe^{II}L^3$_{N14\bullet}$]$^{2+}$, which has an energy = −1,629,502.347 kcal mol^{-1}. Thus, the formation of radical [Fe^{II}L^3$_{N8\bullet}$]$^{2+}$ is favored by 14.9 kcal mol^{-1}. One explanation for this result is the intramolecular hydrogen bonding of the oxygen in the OC$_2$H$_5$ sidearm with the hydrogens of carbon C$_{13}$ (2.30 and 2.65 Å), adjacent to nitrogen N$_{14}$. The angle formed with carbon C$_{15}$, nitrogen N$_{14}$, and carbon C$_{13}$ is 116.08°, while in radical [Fe^{II}L^3$_{N8\bullet}$]$^{2+}$ there is no influence from the OC$_2$H$_5$ sidearm, as indicated by the corresponding angle C$_7$-N$_8$-C$_9$, of 121.27°. The nitrogen atom N$_8$ in the radical [Fe^{II}L^3$_{N8\bullet}$]$^{2+}$ exhibits more sp^2 character, which favors the formation of this radical [20] (Figure 3).

An interesting observation arises from comparing the individual C-H bond lengths in the N$_8$ and N$_{14}$ regions (Table 2). A value of 1.12(2) Å was found for the C$_7$-H$_{7a}$ bond of radical [Fe^{II}L^3$_{N8\bullet}$]$^{2+}$ (vs. 1.11(7) Å for C$_{15}$-H$_{15a}$ in [Fe^{II}L^3$_{N14\bullet}$]$^{2+}$) which is the longest among all the C-H bonds in both [Fe^{II}L^3$_{N14\bullet}$]$^{2+}$ and [Fe^{II}L^3$_{N8\bullet}$]$^{2+}$, and it is this bond that is attacked by dioxygen in the ODH reaction. Analysis of the vibrational frequencies for the methylene groups C$_7$H$_{7a}$H$_{7b}$ and C$_{15}$H$_{15a}$H$_{15b}$ reveals that the C$_7$H$_{7a}$H$_{7b}$ moiety in the radical [Fe^{II}L^3$_{N8\bullet}$]$^{2+}$ has lower frequency values, indicating that this fragment is the most reactive. Note that mono-deuterated carbon atoms C$_7$ and C$_{15}$ of Fe(III) complex (**1**) and corresponding nitrogen radicals (**2a**) have an asymmetric carbon center, as illustrated for radical [Fe^{II}L^3$_{N8\bullet}$]$^{2+}$ (Figure 4) [15].

Additionally, a Natural Bond Orbital (NBO) population analysis has been conducted for the radical (**2a**), with the unpaired electron residing on either nitrogen N$_8$ or N$_{14}$, to obtain the condensed Fukui indices through vertical calculations. They provide insight into the properties of chemical bonds related to their nucleophilic, electrophilic, or radical reactivity [21–26]. The NBO analysis helps us pinpoint the most susceptible site to attack by O$_2$, showing the dual descriptor Δf for the methylene groups of carbon atoms C$_7$ and C$_{15}$ (Table 3). The results indicate that only the hydrogen atom H$_{7a}$ (or deuterium atom D$_{7a}$) of radical [Fe^{II}L^3$_{N8\bullet}$]$^{2+}$ serves as a suitable site for electrophilic attack, with a positive value of

Δf, in contrast to hydrogen atoms H_{15a} and H_{15b} of radical $[Fe^{II}L^3_{N14\bullet}]^{2+}$. The NBO analysis results agree well with our experimental findings, showing that the imine double bond is introduced regio-selectively at position C_7N_8 (Figure 1). Hydrogen atoms H_{7a} and H_{7b} are not equivalent; their Δf values indicate that H_{7a} is the more reactive hydrogen atom (H_{7a} 0.023 vs. H_{7b} 0.012). In calculating the attack of $^3O_2$ on C_7-H_{7b}, after several collisions, the O_2 molecule will orient itself towards the C_7-$H_{7a}\cdots^3O_2$ reaction pathway consistent with the Fukui index analysis (Table 3). The ligand pyridine rings provide electronic repulsion against O_2 attacking C_7-H_b, in favor of the cleavage of the C_7-H_{7a} bond.

Table 2. Calculated bond lengths and vibrational frequencies of the nitrogen radicals $[Fe^{II}L^3_{N8\bullet}]^{2+}$ and $[Fe^{II}L^3_{N14\bullet}]^{2+}$; asymmetric stretching band ν_{as}, symmetric stretching band ν_s.

Isomer	Bond	Length (Å)	Frequency (cm^{-1})
$[Fe^{II}L^3_{N8\bullet}]^{2+}$	N_8-C_7	1.43(8)	
	C_7-H_{7a}	1.12(2)	2937.73 (H_{7a}-C_7-H_{7b} ν_{as})
	C_7-H_{7b}	1.11(7)	2873.72 (H_{7a}-C_7-H_{7b} ν_s)
	N_{14}-C_{15}	1.48(2)	
	C_{15}-H_{15a}	1.11(1)	3023.81 (H_{15a}-C_{15}-H_{15b} ν_{as})
	C_{15}-H_{15b}	1.11(2)	2976.22 (H_{15a}-C_{15}-H_{15b} ν_s)
$[Fe^{II}L^3_{N14\bullet}]^{2+}$	N_8-C_7	1.47(9)	
	C_7-H_{7a}	1.11(1)	3031.81 (H_{7a}-C_7-H_{7b} ν_{as})
	C_7-H_{7b}	1.11(1)	2978.06 (H_{7a}-C_7-H_{7b} ν_s)
	N_{14}-C_{15}	1.44(7)	
	C_{15}-H_{15a}	1.11(7)	2989.45 (H_{15a}-C_{15}-H_{15b} ν_{as})
	C_{15}-H_{15b}	1.11(2)	2924.56 (H_{15a}-C_{15}-H_{15b} ν_s)
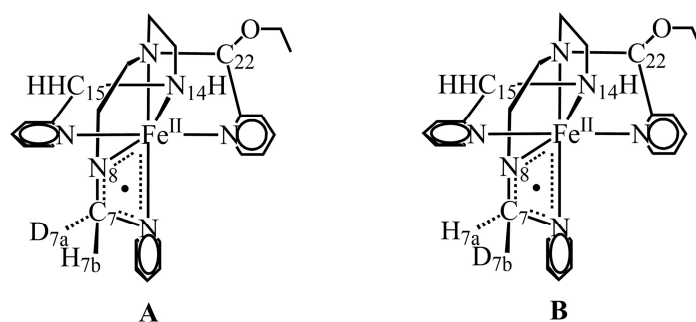
Figure 4. Stereoisomers $[Fe^{II}L^3_{N8\bullet}$–$C_7D_{7a}H_{7b}]^{2+}$ (**A**) and $[Fe^{II}L^3_{N8\bullet}$–$C_7H_{7a}D_{7b}]^{2+}$ (**B**).

Table 3. Fukui indices of selected atoms in radicals $[Fe^{II}L^3_{N8\bullet}]^{2+}$ and $[Fe^{II}L^3_{N14\bullet}]^{2+}$.

Atom	Fukui Indices		
$[Fe^{II}L^3_{N8\bullet}]^{2+}$	f +	f −	Δf
$N_8{}^\bullet$	−0.156	−0.181	0.025
C_7	0.017	0.011	0.006
H_{7b}	−0.030	−0.042	0.012
H_{7a}	−0.038	−0.061	0.023
C_6	0.010	0.015	−0.005
$[Fe^{II}L^3_{N14\bullet}]^{2+}$	f +	f −	Δf
$N_{14}{}^\bullet$	−0.200	−0.099	−0.101
C_{15}	0.016	0.011	0.005
H_{15a}	−0.024	−0.025	0.001
H_{15b}	−0.038	−0.026	−0.012
C_{16}	0.006	0.001	0.005

2.3. Hydrogen Atom Transfer $[Fe^{II}L^3{}_{N8\bullet}]^{2+} + {}^3O_2 \rightarrow [Fe^{II}L^4]^{2+} + HO_2{}^\bullet$

2.3.1. Transition State $\{[Fe^{II}L^3{}_{N8\bullet\ C7\bullet}]^{2+}\text{---}H_{7a}\text{---}{}^3O_2\}$

In the transition state $\{[Fe^{II}L^3{}_{N8\bullet\ C7\bullet}]^{2+}\text{---}H_{7a}\text{---}{}^3O_2\}$ (M = 4) (Figure 5), the interaction with ${}^3O_2$ (M = 3) defines the C_7H_{7a}-O_2 angular geometry, with distances Fe-O_2 4.02 Å, O-O 1.30 Å vs. starting distances Fe-O_2 4.06 Å, O-O 1.21 Å. The intramolecular hydrogen bond between the oxygen and the methylene $C_{12}H_{12a}H_{12b}$ group (distance O---H 2.33 Å, bond angle 98.4°) will enhance the structural stability of the $\{[Fe^{II}L^3{}_{N8\bullet\ C7\bullet}]^{2+}\text{---}H_{7a}\text{---}{}^3O_2\}$ transition state. Steric crowding from the peripheral atoms restricts O_2 access to the metal center, inhibiting the formation of high-valent Fe-oxo species (Figure 3).
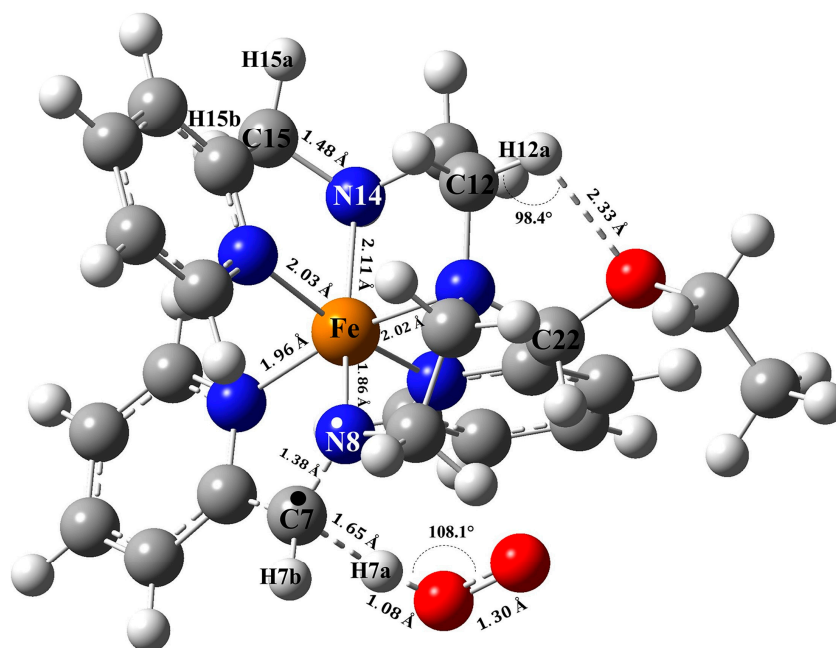
Figure 5. Optimized structure of the transition state $\{[Fe^{II}L^3{}_{N8\bullet\ C7\bullet}]^{2+}\text{---}H_{7a}\text{---}{}^3O_2\}$ (M = 4); TS distances Fe–O_2 4.02 Å, C_7H_{7a}–O_2 1.08 Å, O–O 1.30 Å vs. starting distances Fe–O_2 4.06 Å, O–O 1.21 Å; Fe orange, H white, C grey, N blue, O red.

2.3.2. Spin Density, Charge Density, and Frontier Orbitals

Valuable information on the radical $[Fe^{II}L^3{}_{N8\bullet}]^{2+}$ and its reactivity towards ${}^3O_2$ (M = 3) is derived from the spin density population analysis (Figure 6). In the starting complex $[Fe^{III}L^3]^{3+}$ (**1**, state (i)), the spin density of the unpaired electron is entirely localized on the Fe(III) center, with no significant contributions from other atoms in the molecule. In state (ii)/(iii), after deprotonation of the N_8-H bond in complex (**1**), the radical $[Fe^{II}L^3{}_{N8\bullet}]^{2+}$ (**2a**) (M = 2) is formed, with the spin density mainly found on the metal via delocalization between Fe(II) and nitrogen atom N_8 (Table A1), with a negative, close to zero, value on the target carbon C_7; O_2 in the vicinity of $[Fe^{II}L^3{}_{N8\bullet}]^{2+}$, with a non-bonding distance of ≈ 2 Å, does not lead to a significant change in spin density distribution. In state (iv), when O_2 is in the proximity of $[Fe^{II}L^3{}_{N8\bullet}]^{2+}$, the transition state is formed through the hydrogen atom H_{7a} positioned between carbon C_7 and O_2 (Figure 5); spin density is transferred from O_2 to the Fe(II) radical while H_{7a} is detached from C_7, which significatively increases the spin density on carbon C_7. Remarkably, in the transition state, the Fe(II) complex shows a biradical character, as outlined in the proposed reaction mechanism (Figure 2). Finally, in state (v), the H_{7a} atom is no longer bound to C_7, and the diamagnetic final product, mono-imine complex, $[Fe^{II}L^4]^{2+}$, (**2**) (M = 1) is formed with the consecutive release of $HO_2{}^\bullet$. In summary, spin and charge density transfer analysis provides an important

contribution to our understanding of the ODH reaction, with $^3O_2$ as an oxidant, following the HAT mechanism.

(A)

(B)
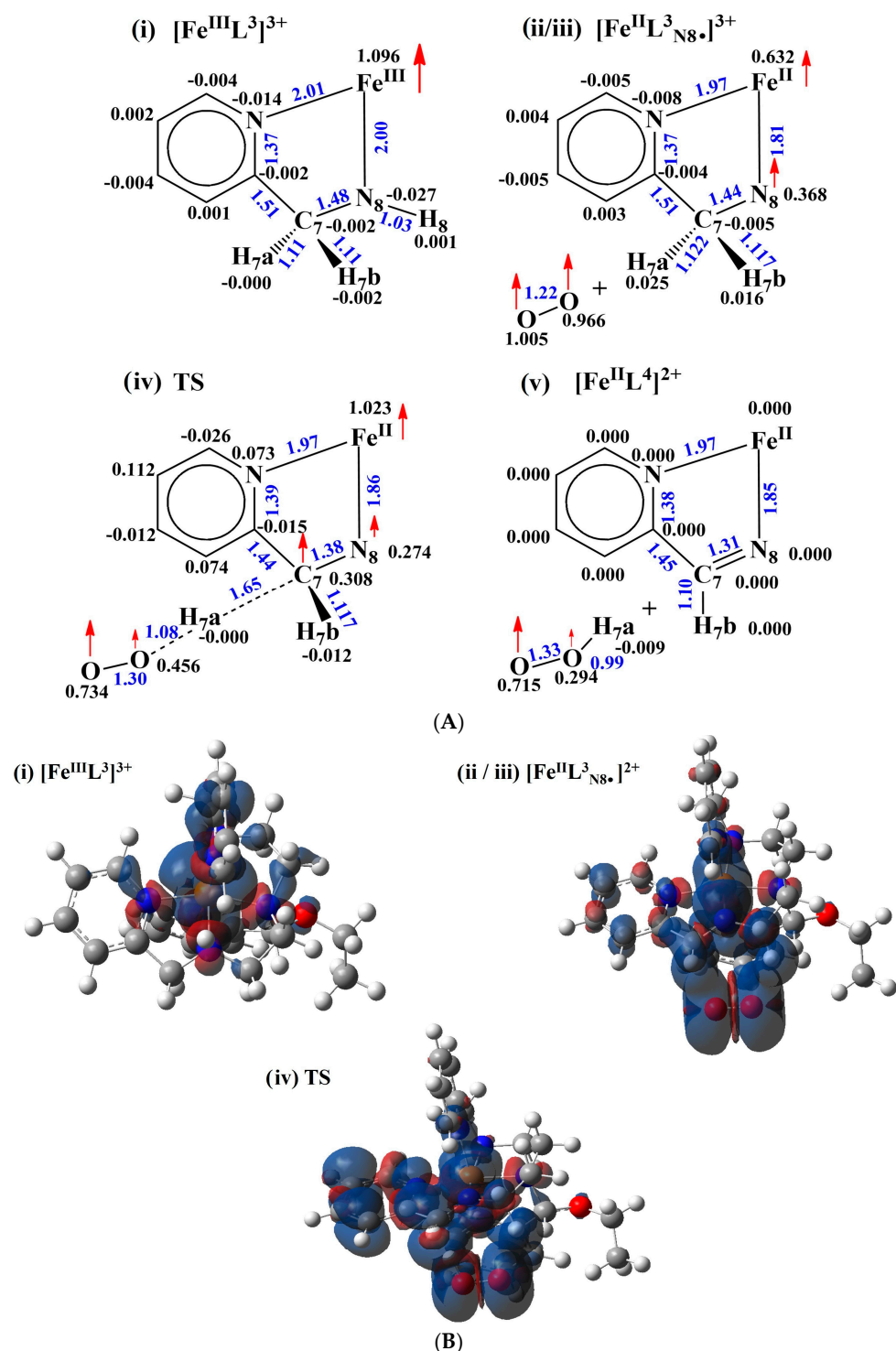
Figure 6. (**A**). Spin density population analysis of the reactive fragments of $[Fe^{II}L^3_{N8\bullet}]^{2+}$, (**2a**) (M = 2) and $^3O_2$ (M = 3) undergoing hydrogen atom transfer; spin density values in black, bond lengths (Å) in blue. (**B**). Spin density contour plots for the reactive fragments of $[Fe^{II}L^3_{N8\bullet}]^{2+}$, (**2a**) (M = 2) and $^3O_2$ (M = 3) undergoing hydrogen atom transfer; the imine product, $[Fe^{II}L^4]^{2+}$, species (v) in (**A**), has zero spin and is diamagnetic (M = 1); blue region, spin up; red region, spin down.

Next, the Natural Bond Order approach has been used to study the transfer of charge from $[Fe^{II}L^3_{N8\bullet}]^{2+}$ (M = 2) to $^3O_2$ (M = 3) (Figure 7). Analysis of the initial Fe(III) complex (**1**, state (i)) shows a large charge value located on Fe(III) (+0.657e). Notably, Fe(III) induces

the polarization of the coordinated amine N_8 ($-0.592e$)-H_8 ($+0.432e$), with H_8 susceptible to deprotonation. The nitrogen radical (ii)/(iii) shows the delocalization of the electron density over the methylpyridine fragment, with the larger values on Fe(II) ($+0.447e$) and the coordinated N atoms ($-0.418e/-0.425e$); additionally, carbon C_7 shows a value of $-0.274e$, which indicates its tendency to donate electrons. At a distance of 2.0 Å between $^3O_2$ and radical (**2a**) the partial charges do not change. In transition state (iv) (Figure 5), charge transfer occurs from (**2a**) to $^3O_2$; this process begins through the C_7-H_{7a} moiety. As a result, both the carbon atom C_7 and the hydrogen atom H_{7a} become more positively charged. The negative charge on the oxygen atoms increases significantly ($-0.223e$, $-0.152e$) showing a partial reduction of the O_2 molecule, while N_8 becomes more negative. As H_{7a} is detached from C_7 in the transition state, the values on C_7 and H_{7a} increase, showing the electron density donation from the C_7-H_{7a} fragment towards O_2. Note that part of the initial electron density of the C_7-H_{7a} bond shifts towards nitrogen N_8. Finally, in stage (v), the H_{7a} atom is no longer bound to C_7, and $HO_2^\bullet$ is formed. In summary, spin and charge density transfer analysis provides an important contribution to our understanding of the ODH reaction, with $^3O_2$ as an oxidant, following the HAT mechanism.
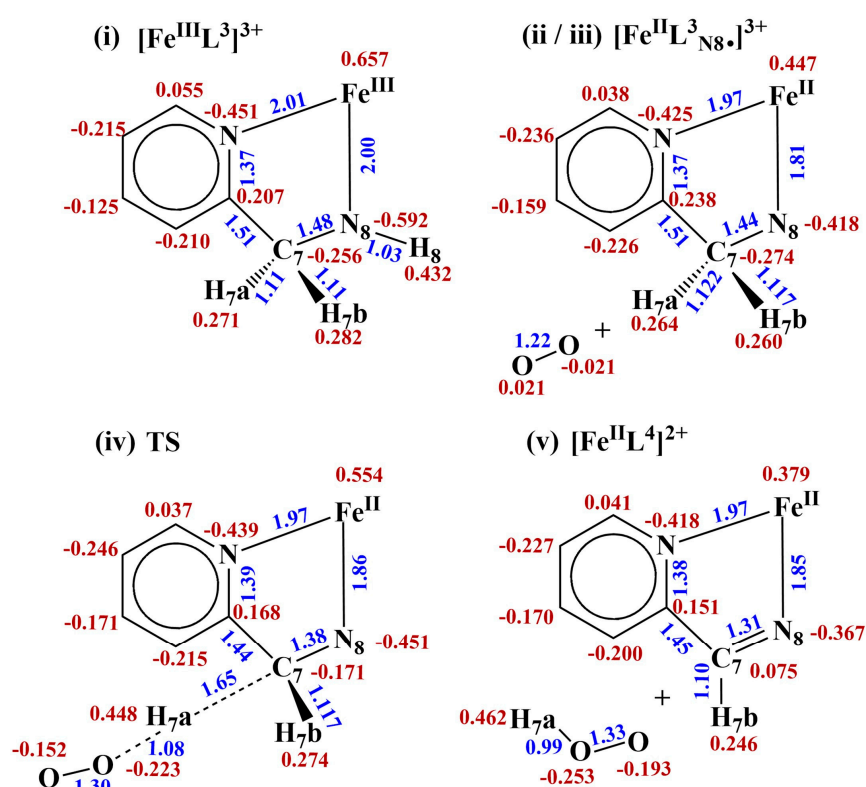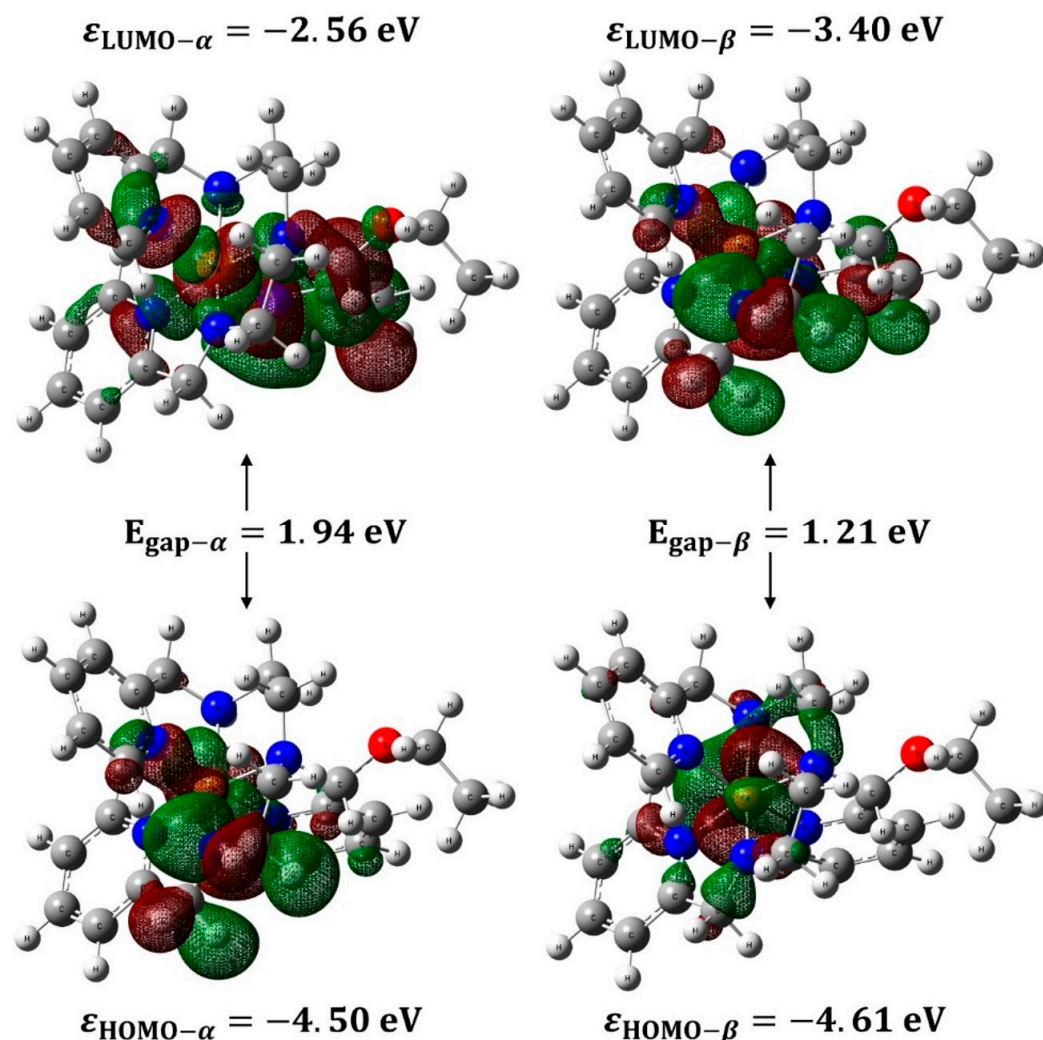

Figure 7. Natural Bond Order charge population analysis of the reactive fragment of $[Fe^{II}L^3{}_{N8\bullet}]^{2+}$, (**2a**) (M = 2) and $^3O_2$ (M = 3) undergoing hydrogen atom transfer; charge population red, bond length (Å) blue.

An important aspect highlighted in the NBO charge population analysis (Figure 7) concerns the charge transfer from C_7H_{7a} to $^3O_2$ in the transition state (M = 4), involving 0.37 electrons. The HOMO orbitals of the $[Fe^{II}L^3{}_{N8\bullet})]^{2+}$ radical (A) exhibit signatures in the C_7H_{7a} region, which is where $^3O_2$ interacts (Figure 8). As an open-shell system, $[Fe^{II}L^3{}_{N\bullet}]^{2+}$ (M = 2) has two different possibilities for the molecular orbitals arising from its spin configuration. These are α and β, giving two pairs of frontier molecular orbitals HOMO-α/LUMO-α and HOMO-β/LUMO-β, with an energy difference of 0.11 eV (2.5367 kcal mol^{-1}) between HOMO-α and HOMO-β. Thus, both orbitals might contribute to transferring electrons of C_7H_{7a} to $^3O_2$ in the transition state. For the LUMO-α and

LUMO-β orbitals, we observe an energy gap of 0.84 eV (19.37 kcal mol^{-1}), with LUMO-β showing a greater propensity to accept electrons from O_2 in the region where the imine bond is formed. The significantly lower energy gap of 1.21 eV (27.90 kcal mol^{-1}) for HOMO-β and LUMO-β, compared to 1.94 eV (44.74 kcal mol^{-1}) for HOMO-α and LUMO-α, suggests that HOMO-β and LUMO-β play a major role in charge transfer. This transfer occurs from C_7H_{7a} to O_2 and from O_2 back to C_7H_{7a} during the imine formation process.

$$\varepsilon_{LUMO-\alpha} = -2.56 \text{ eV} \qquad \varepsilon_{LUMO-\beta} = -3.40 \text{ eV}$$

$$E_{gap-\alpha} = 1.94 \text{ eV} \qquad E_{gap-\beta} = 1.21 \text{ eV}$$

$$\varepsilon_{HOMO-\alpha} = -4.50 \text{ eV} \qquad \varepsilon_{HOMO-\beta} = -4.61 \text{ eV}$$

Figure 8. Frontier orbitals (HOMO–LUMO) of nitrogen radical [Fe^{II}L^3$_{N8\bullet}$]$^{2+}$ (**2a**). The significantly lower energy gap of 1.21 eV for HOMO–β and LUMO–β, compared to 1.94 eV for HOMO–α and LUMO–α, suggests that HOMO–β and LUMO–β play a major role in charge transfer, occurring from C_7H_{7a} to O_2 and from O_2 back to C_7H_{7a} during the imine formation process. Green and red stands for the bonding and antibonding regions of the frontier HOMO and LUMO molecular orbitals.

3. Discussion

Extensive kinetic studies have led to the development of a mechanism for the oxidative dehydrogenation (ODH) of [Fe^{III}L^3]$^{3+}$ (**1**), using O_2 as the oxidant. This mechanism identifies the radical [Fe^{II}L^3$_{N8\bullet}$]$^{2+}$ as a crucial component and follows the hydrogen atom transfer (HAT) pathway (see Figure 2; kinetic equations including the final third-order rate law can be found in A2) [15]. As mentioned, a C-H KIE k^{CH}/k^{CD} with a value of 2.30 was observed for the rate-determining step of the ODH reaction when using the deuterated pyridyl-amine ligand L^3-D.

The nitrogen radical reacts with $^3O_2$, resulting in the transition state denoted as {[Fe^{II}L^3$_{N8\bullet\ C7\bullet}$]$^{2+}$---H$_{7a}$---$^3O_2$}. In this state, the spin density is observed on nitrogen

N_8 (0.274) and carbon C_7 (0.308) (Figure 6A). This is followed by the formation of a C_7N_8 double bond in the final mono-imine product $[Fe^{II}L^4]^{2+}$, along with the release of $HO_2^{\bullet}$. In the transition state, the hydrogen atom H_{7a} is intermediate between C_7 and O_2, defining the reaction coordinate C_7---H_{7a}---O_2, with an associated stretching imaginary vibrational frequency of -390 cm^{-1}. It's important to emphasize that the transition state has just one imaginary frequency, as this is precisely what we anticipate in such cases.

There is no evidence for the formation of a high-valent iron-oxo species, likely because the metal center in $[Fe^{III}L^3]^{3+}$ and $[Fe^{II}L^3_{N8\bullet}]^{2+}$ is deeply buried (Figure A1). This species is a key player in nonheme iron dioxygenases that perform C-H oxidation reactions by transferring hydrogen atoms to the $[Fe^{IV}=O]^{2+}$ site [27–31].

The data compiled in Table 1 allow us to calculate the energy profile of the ODH reaction, including the activation parameters for the formation of the mono-imine $[Fe^{II}L^4]^{2+}$ by the HAT mechanism (Figure 9). The activation energy, E_a (Δ EE + ZPE TS—reactants) = 19.34 kcal mol^{-1}, and the activation parameters $\Delta H^{\neq}$ (Δ EE + TEC TS—reactants) = 19.19 kcal mol^{-1} and $\Delta S^{\neq}$ (ΔS TS—reactants) = -0.034 kcal mol^{-1} K^{-1}. These estimated values are close to the experimental results, E_a = 21.04 kcal mol^{-1}, $\Delta H^{\neq}$ = 20.38 kcal mol^{-1} and $\Delta S^{\neq}$ = -0.018 kcal mol^{-1} K^{-1} (Figure 9) [15].
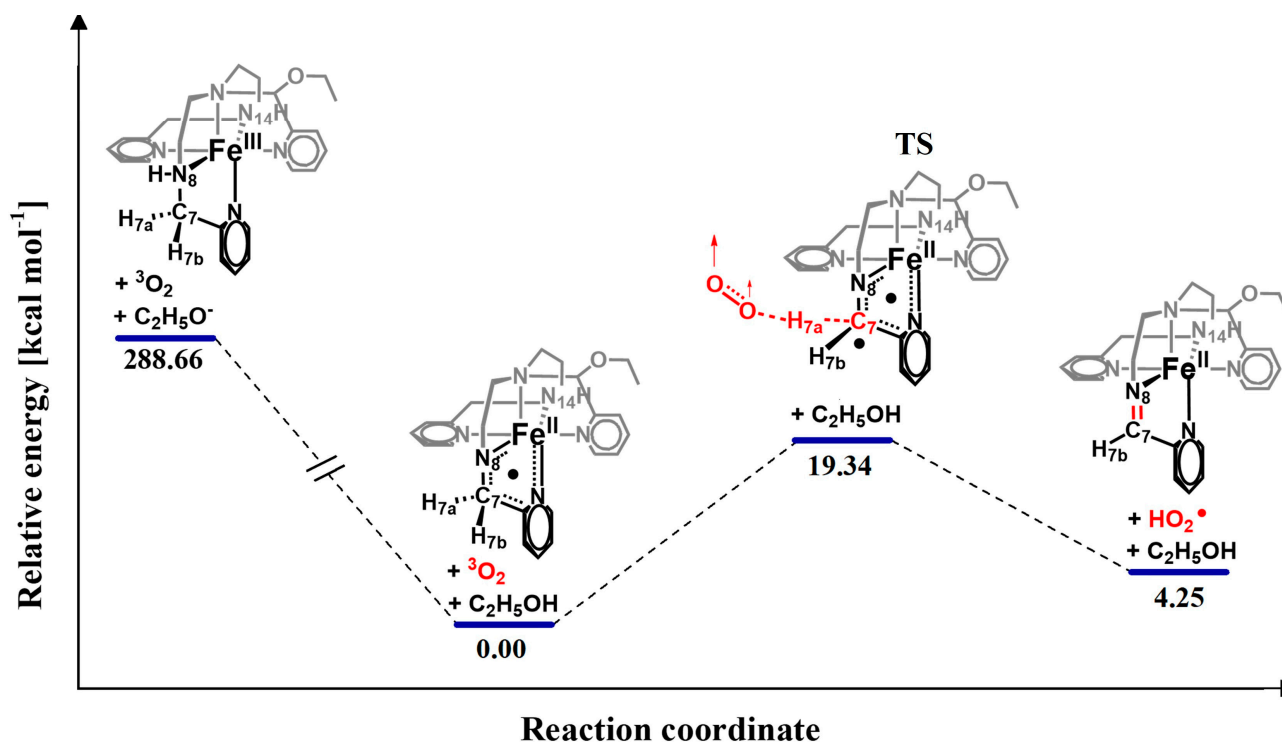
Figure 9. Energy profile calculated for the ODH reaction $[Fe^{III}L^3]^{3+}$ + $^3O_2$ + $C_2H_5O^-$ → $[Fe^{II}L^4]^{2+}$ + $HO_2^{\bullet}$ + C_2H_5OH (see HAT mechanism outlined in Figure 2); E_a = 19.34 kcal mol^{-1}; $\Delta H^{\neq}$ = 19.19 kcal mol^{-1}; $\Delta S^{\neq}$ = -0.034 kcal mol^{-1} K^{-1}. Electronic energies corrected for ZPE (Table 1).

The amine-imine oxidation reaction discussed in this work (Figure 1) starts with the deprotonation of the N_8-H bond in $[Fe^{III}L^3]^{3+}$ (**1**), resulting in the formation of the nitrogen radical $[Fe^{II}L^3_{N8\bullet}]^{2+}$ (**2a**), a key player in the process. The main themes of this process are typical to many amine-imine oxidations involving Ru(II) and Fe(III) complexes. Two basic types of mechanisms have been proposed for the amine-imine 2e$^-$/2H$^+$ transfer process [14]: (i) 2e$^-$-step reactions involving high-valent metal centers [27–31], and (ii) 1e$^-$-step reactions involving ligand-radical intermediates [32–36]. Nevertheless, the reaction from $[Fe^{III}L^3]^{3+}$ (**1**) to $[Fe^{II}L^4]^{2+}$ (**2**) was noted as novel since it occurred spontaneously

without requiring an external oxidant, and it appeared representative of similar systems involving fundamental proton and electron transfer steps [37].

The interest in the (bio)chemistry of radicals, transient or stable, has skyrocketed over the past four decades [38,39]. In particular, the chemistry of nitrogen-centered radicals has found plentiful applications in organic synthesis, which is not surprising since the nitrogen atom is common in many important (bio)molecules and is essential for fine-tuning their physicochemical properties [20,40,41]. Metal-coordinated nitrogen-centered radicals are generally more stable than free organic nitrogen-centered radicals; thus they open the door to powerful catalytic applications [42,43]. In metal radical complexes, the localization of the unpaired electron can take on distinct forms. It may reside predominantly at the nitrogen atom, resulting in aminyl radicals (designated as LM^{m+}-$N^{\bullet}R_2$), or it may be associated with the metal itself, as seen in amidyl radicals (indicated as LM^{m+1}-$N^{\bullet\bullet}R_2$). This key distinction is exemplified in the aminyl radical Rh(I) complex, which shows reactivity with a variety of hydrogen atom donors [42]. The topic has been meticulously discussed by Kaim, shedding light on the nuances of these fascinating complexes with redox-active ligands showing non-innocent behavior [44].

The computational analysis of the Fe(III)-promoted oxidative dehydrogenation of amines supports the findings of the kinetic results [15]. We demonstrate that the cleavage of the C-H bond occurs through a hydrogen atom transfer (HAT) mechanism. The nitrogen radical $[Fe^{II}L^3N_{8\bullet}]^{2+}$ (**2a**) plays a crucial role in the regio-selective abstraction of hydrogen atoms by O_2, leading to the subsequent formation of the hydroperoxyl radical, $HO_2^{\bullet}$. In summary, understanding the Fe(III)-promoted ODH reaction enhances catalyst development for controlled C-H bond activation and functionalization, which remains a major challenge in synthetic chemistry.

4. Materials and Methods

The Fe(III)-promoted ODH reaction in the presence of O_2 as oxidant, and the radical $[Fe^{II}L^3_{N8\bullet}]^{2+}$ (**2a**) as key intermediate, was analyzed using density functional theory (DFT). All electron calculations were performed at the PBE level of theory [45–47], coupled with Def2SVP basis sets and including GD3 empirical dispersion correction [48–50]. The quantum chemical software Gaussian 09 was used [19]. The geometry of the radical (**2a**) was established based on the X-ray structure of $[Fe^{II}L^4][B(C_6H_5)_4]_2$ (**2**) [12,13], CCDC reference number 286407. This initial structure was relaxed using a geometry optimization procedure. A strict convergence criterion was applied for the total energy minimized to 10^{-8} a.u.; structures were relaxed with 10^{-5} eV/Å as a threshold criterion for force convergence. The interaction of $^3O_2$, (M = 3), with $[Fe^{II}L^3_{N8\bullet}]^{2+}$ (**2a**) (M = 2) was analyzed for structures of different geometries and multiplicities. Several pathways of O_2, approaching the C-H/C-D groups, were investigated to identify the most energetically favorable configuration for H/D atom transfer $[Fe^{II}L^3_{N8\bullet}]^{2+} \rightarrow {}^3O_2$, resulting in the formation of the Fe(II) imine complex (**2**) and the O_2H/D radical. We employed conceptual DFT to study the electronic and structural properties and the chemical reactivity of the systems of interest (atomic charge, condensed Fukui index, Natural Bond Orbital population analysis, dual descriptor, and HOMO-LUMO gap, SI). To test and calibrate the procedure, we calculated (i) the structure and ground state of the Fe(II) imine complex (**2**) and (ii) the molecular geometry of the hydroperoxyl radical $HO_2^{\bullet}$, with results in excellent agreement with the reported experimental data [12,13,51].

5. Conclusions

Many biological and chemical processes employ dioxygen as an oxidant, involving metal-dependent C−H activation and functionalization as critical steps. One prime exam-

ple is the heme-dependent enzyme cytochrome P450, a catalyst with a remarkable substrate range and an enormous potential for industrial applications [52]. Exploring its reaction mechanism through chemical, spectroscopic, and computational methods has resulted in significant research aimed at developing efficient catalytic systems [53]. Non-heme iron complexes, particularly those with pyridyl-alkylamine ligands, have received significant attention due to their inspiration from the active sites of metalloenzymes [27–30]. In this research, we have performed a DFT theoretical study to enhance our understanding of the oxygen-dependent dehydrogenation of the Fe(III) pyridyl-amine complex (**1**) into the stable Fe(II) mono-imine complex (**2**). Before the computational studies, the reaction was thoroughly investigated using kinetic methods, multinuclear NMR spectroscopy, and X-ray crystallography. It has been proposed that the cleavage of the C-H bond occurs via hydrogen atom transfer (HAT) [15]. High-valent Fe oxo species are not observed in the dehydrogenation reaction because steric hindrance from surrounding atoms prevents the direct coordination of O_2 with the iron center. The preferred site for the O_2 attack on the nitrogen radical $[Fe^{II}L^3_{N8\bullet}]^{2+}$ has been identified, which plays a crucial role in the hydrogen atom transfer (HAT) mechanism. It allows for regio-selective hydrogen atom abstraction by O_2, ultimately resulting in the formation of the hydroperoxyl radical $HO_2^{\bullet}$ in line with the experimental findings. The theoretical results regarding the transition state indicate significant effects related to the transfer of spin density from the O_2 molecule to $[Fe^{II}L^3_{N8\bullet}]^{2+}$, which defines the reactive site in the hydrogen atom transfer (HAT) mechanism. Additionally, the charge transfer to the O_2 molecule also is important in the reaction HAT step. The calculated transition state is characterized by notable spin populations on the C_7 atom and the N_8 atom of the ligand, suggesting the formation of a biradical species. The calculated parameters align closely with the experimental values: activation energy (E_a) is 19.34 kcal mol^{-1} vs. 21.04 kcal mol^{-1}; the enthalpy of activation ($\Delta H^{\neq}$) is 19.19 kcal mol^{-1} vs. 20.38 kcal mol^{-1}; and the entropy of activation ($\Delta S^{\neq}$) is -0.034 kcal mol^{-1} K^{-1} vs. -0.018 kcal mol^{-1} K^{-1}. These results underscore the reliability of the computational approach and convincingly document the role of computational chemistry as an integral and essential component of chemical research [54].

Author Contributions: Conceptualization, M.E.S.-T.; methodology, R.D.P.-L., A.S.-P., H.F.C.-H., M.Á.G.-S. and M.C.; investigation, R.D.P.-L., A.S.-P., H.F.C.-H., M.Á.G.-S. and M.C.; writing—original draft preparation, M.E.S.-T. and P.M.H.K.; writing—review and editing, R.D.P.-L., M.E.S.-T., M.C. and P.M.H.K.; supervision, M.E.S.-T. and M.C.; project administration, M.E.S.-T. and M.C.; funding acquisition, M.E.S.-T. and M.C. All authors have read and agreed to the published version of the manuscript.

Data Availability Statement: The X-ray coordinates of mono-imine complex $[Fe^{II}L^4][C_6H_5)_4]_2$ can be found on the Cambridge Structural Database (CCDC-286407). The original contributions presented in the study are included in the article; further inquiries can be directed to the corresponding author.

Conflicts of Interest: The authors declare no conflicts of interest.

Appendix A
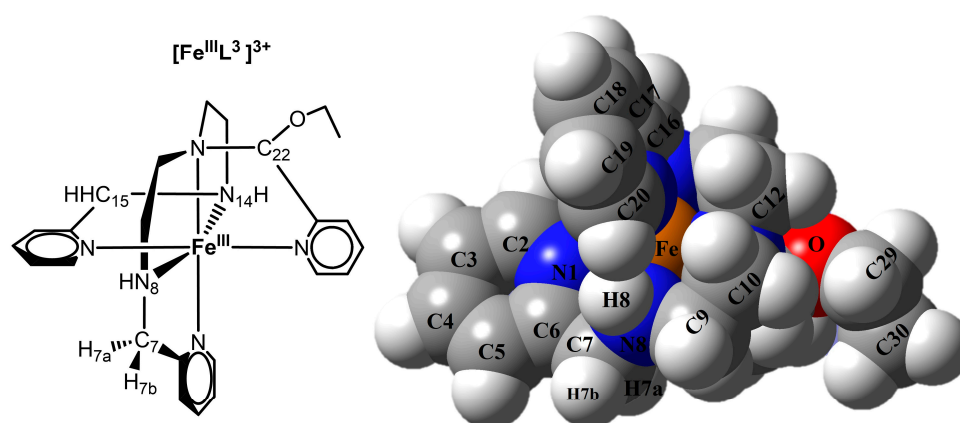
Figure A1. Optimized structure of Fe(III) complex (**1**) $[Fe^{III}L^3]^{3+}$ calculated with Gaussian 09 (DFT-PBEPBE-Def2SVP) using the X-ray coordinates of $[Fe^{II}L^4][C_6H_5)_4]_2$ (CCDC-286407); Fe orange, H white, C grey, N blue, O red.

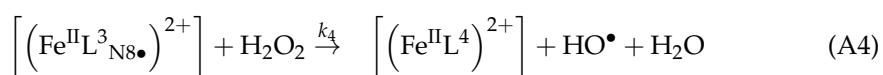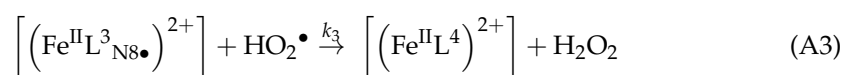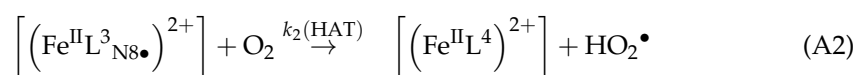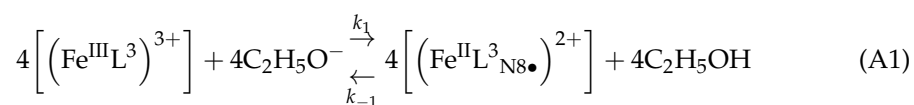**Table A1.** Spin density population for selected atoms of nitrogen radicals $[Fe^{II}L^3_{N8\bullet}]^{2+}$ and $[Fe^{II}L^3_{N14\bullet}]^{2+}$ shown in Figure 3. Note that the N_{14} site has a slightly larger spin density (0.379) than N_8 (0.359). However, the Fukui function results indicate that N_8 is the preferred reactive site, consistent with the fact that the $[Fe^{II}L^3_{N8\bullet}]^{2+}$ radical is 14.9 kcal mol^{-1} more stable.

$[Fe^{II}L^3_{N8\bullet}]^{2+}$		$[Fe^{II}L^3_{N14\bullet}]^{2+}$	
Atom	**Spin Density**	**Atom**	**Spin Density**
Fe	0.628	Fe	0.638
$N_8{}^\bullet$	0.359	$N_{14}{}^\bullet$	0.379
C_7	−0.021	C_{15}	−0.019
H_{7a}	0.034	H_{15a}	0.021
H_{7b}	0.015	H_{15b}	−0.001
N_{14}	−0.011	N_8	−0.008
H_{14}	0.001	H_8	0.000
C_{15}	0.002	C_7	0.004
H_{15a}	0.000	H_{7a}	0.000
H_{15b}	0.000	H_{7b}	0.003

Third-Order Rate law A2. Kinetic equations developed for the oxidative dehydrogenation of Fe(III) complex (**1**) $[Fe^{III}L^3]^{3+}$, with O_2 as an oxidant.

$$4\left[\left(Fe^{III}L^3\right)^{3+}\right] + 4C_2H_5O^- \underset{k_{-1}}{\overset{k_1}{\rightleftarrows}} 4\left[\left(Fe^{II}L^3_{N8\bullet}\right)^{2+}\right] + 4C_2H_5OH \tag{A1}$$

$$\left[\left(Fe^{II}L^3_{N8\bullet}\right)^{2+}\right] + O_2 \overset{k_2(HAT)}{\rightarrow} \left[\left(Fe^{II}L^4\right)^{2+}\right] + HO_2{}^\bullet \tag{A2}$$

$$\left[\left(Fe^{II}L^3_{N8\bullet}\right)^{2+}\right] + HO_2{}^\bullet \overset{k_3}{\rightarrow} \left[\left(Fe^{II}L^4\right)^{2+}\right] + H_2O_2 \tag{A3}$$

$$\left[\left(Fe^{II}L^3_{N8\bullet}\right)^{2+}\right] + H_2O_2 \overset{k_4}{\rightarrow} \left[\left(Fe^{II}L^4\right)^{2+}\right] + HO^\bullet + H_2O \tag{A4}$$

$$\left[\left(Fe^{II}L^3_{N8\bullet}\right)^{2+}\right] + HO^\bullet \overset{k_5}{\rightarrow} \left[\left(Fe^{II}L^4\right)^{2+}\right] + H_2O \tag{A5}$$
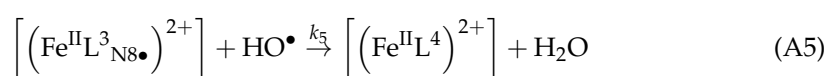
Applying the steady-state approximation to the radical species $[(Fe^{II}L^3{}_{N8\bullet})]^{2+}$ results in Equation (A6).

$$-\frac{d\left[\left(Fe^{III}L^3\right)^{3+}\right]}{dt} = \frac{4k_1 k_2 \left[\left(Fe^{III}L^3\right)^{3+}\right][O_2]\left[C_2H_5O^-\right]}{k_{-1} - 4k_2[O_2]} \tag{A6}$$

Within the limit $k_{-1} \gg k_2[O_2]$, the rate law in Equation (A6) simplifies to the rate law presented in Equation (A7), consistent with the experimentally determined third-order rate equation; k_1/k_{-1} is the acid-base equilibrium constant K, resulting in the final rate law and k_2 is the rate-determining step (Equation (A8)).

$$-\frac{d\left[\left(Fe^{III}L^3\right)^{3+}\right]}{dt} = \frac{4k_1 k_2}{k_{-1}}\left[\left(Fe^{III}L^3\right)^{3+}\right][O_2]\left[C_2H_5O^-\right] \tag{A7}$$

$$-\frac{d\left[\left(Fe^{III}L^3\right)^{3+}\right]}{dt} = 4\,K k_2 \left[\left(Fe^{III}L^3\right)^{3+}\right][O_2]\left[C_2H_5O^-\right] \tag{A8}$$

References

1. Crichton, R.R. *Biological Inorganic Chemistry. A New Introduction to Molecular Structure and Function*, 3rd ed.; Academic Press: Cambridge, MA, USA, 2019. [CrossRef]
2. Solomon, E.I.; Goudarzi, S.; Sutherlin, K.D. O_2 Activation by Non-Heme Iron Enzymes. *Biochemistry* **2016**, *55*, 6363–6374. [CrossRef]
3. Maret, W. Zinc Biochemistry: From a Single Zinc Enzyme to a Key Element of Life. *Adv. Nutr.* **2013**, *4*, 82–91. [CrossRef] [PubMed]
4. Koschorreck, K.; Alpdagtas, S.; Urlacher, V.B. Copper-radical oxidases: A diverse group of biocatalysts with distinct properties and a broad range of biotechnological applications. *Appl. Eng. Microbiol.* **2022**, *2*, 100037. [CrossRef] [PubMed]
5. Jiao, Y.; Chen, X.-Y.; Stoddart, J.F. Weak bonding strategies for achieving regio- and site-selective transformations. *Chem* **2022**, *8*, 414–438. [CrossRef]
6. Dalton, T.; Faber, T.; Glorius, F. C−H Activation: Toward Sustainability and Applications. *ACS Cent. Sci.* **2021**, *7*, 245–261. [CrossRef]
7. Kumar Sinha, S.; Guin, S.; Maiti, S.; Prasad Biswas, J.; Porey, S.; Maiti, D. Toolbox for Distal C−H Bond Functionalizations in Organic Molecules. *Chem. Rev.* **2022**, *122*, 5682–5841. [CrossRef]
8. Budweg, S.; Wei, Z.; Jiao, H.; Junge, K.; Beller, M. Iron-PNP Pincer-Catalyzed Transfer Dehydrogenation of Secondary Alcohols. *ChemSusChem* **2019**, *12*, 2988–2993. [CrossRef] [PubMed]
9. Sinha, S.; Das, S.; Sikari, R.; Parua, S.; Brandaõ, P.; Demeshko, S.; Meyer, F.; Paul, N.D. Redox Noninnocent Azo-Aromatic Pincers and Their Iron Complexes. Isolation, Characterization, and Catalytic Alcohol Oxidation. *Inorg. Chem.* **2017**, *56*, 14084–14100. [CrossRef]
10. Darcy, J.W.; Koronkiewicz, B.; Parada, G.A.; Mayer, J.M. A Continuum of Proton-Coupled Electron Transfer Reactivity. *Acc. Chem. Res.* **2018**, *51*, 2391–2399. [CrossRef] [PubMed]
11. Ugalde-Saldívar, V.M.; Sosa-Torres, M.E.; Ortiz-Frade, L.; Bernès, S.; Höpfl, H. Novel iron(II) complexes with hexadentate nitrogen ligands obtained via intramolecular redox reactions. *Dalton Trans.* **2001**, *20*, 3099–3107. [CrossRef]
12. Saucedo-Vázquez, J.P.; Ugalde-Saldívar, V.M.; Toscano, A.R.; Kroneck, P.M.H.; Sosa-Torres, M.E. On the Mechanism of Iron(III)-Dependent Oxidative Dehydrogenation of Amines. *Inorg. Chem.* **2009**, *48*, 1214–1222. [CrossRef] [PubMed]
13. Saucedo-Vázquez, J.P.; Kroneck, P.M.H.; Sosa-Torres, M.E. The role of molecular oxygen in the iron(III)-promoted oxidative dehydrogenation of amines. *Dalton Trans.* **2015**, *44*, 5510–5519. [CrossRef]
14. Keene, F.R. Metal-ion promotion of the oxidative dehydrogenation of coordinated amines and alcohols. *Coord. Chem. Rev.* **1999**, *187*, 121–149. [CrossRef]
15. Páez-López, R.D.; Gómez-Soto, M.Á.; Cortés-Hernández, H.F.; Solano-Peralta, A.; Castro, M.; Kroneck, P.M.H.; Sosa-Torres, M.E. Fe(III)-promoted oxidative dehydrogenation of amines by O_2—mediated cleavage of C-H bond proceeds via hydrogen atom transfer (HAT). *Inorg. Chim. Acta* **2025**, *578*, 122516. [CrossRef]
16. Victória, H.F.; Ferreira, D.C.; José Filho, B.G.; Martins, D.C.; Pinheiro, M.V.; de AMSáfar, G.; Krambrock, K. Detection of singlet oxygen by EPR: The instability of the nitroxyl radicals. *Free Rad. Biol. Med.* **2022**, *180*, 143–152. [CrossRef]

17.	Peng, H.-L.; Chen, X.-Y.; Li, L.-P.; Ye, B.-H. Mechanism study on photo-oxidation dehydrogenation of cyclometalated Ir (III) amino acid complexes. *Inorg. Chim. Acta* **2020**, *513*, 119939. [CrossRef]

18.	Zheng, N.; He, X.; Hu, R.; Wang, R.; Zhou, Q.; Lian, Y.; Hu, Z. In-situ production of singlet oxygen by dioxygen activation on iron phosphide for advanced oxidation processes. *Appl. Catal. B Environ.* **2022**, *307*, 121157. [CrossRef]

19.	Frisch, M.J.; Trucks, G.W.; Schlegel, H.B.; Scuseria, G.E.; Robb, M.A.; Cheeseman, J.R.; Scalmani, G.; Barone, V.; Mennucci, B.; Petersson, G.A.; et al. *Gaussian 09*, Revision A.02; Gaussian, Inc.: Wallingford, CT, USA, 2009.

20.	Gao, S.; Li, F. Neutral Stable Nitrogen-Centered Radicals: Structure, Properties, and Recent Functional Application Progress. *Adv. Funct. Mater.* **2023**, *33*, 2304291. [CrossRef]

21.	Weinhold, F. Natural bond orbital analysis: A critical overview of relationships to alternative bonding perspectives. *J. Comp. Chem.* **2012**, *33*, 2363–2379. [CrossRef]

22.	Glendening, E.D.; Hiatt, D.M.; Weinhold, F. Natural Bond Orbital Analysis of Chemical Structure, Spectroscopy, and Reactivity: How it Works. *Compr. Comput. Chem.* **2024**, *2*, 406–421. [CrossRef]

23.	Reed, A.E.; Curtiss, L.A.; Weinhold, F. Intermolecular interactions from a natural bond orbital, donor-acceptor viewpoint. *Chem. Rev.* **1988**, *88*, 899–926. [CrossRef]

24.	Zamora, P.P.; Bieger, K.; Cuchillo, A.; Tello, A.; Muena, J.P. Theoretical determination of a reaction intermediate: Fukui function analysis, dual reactivity descriptor and activation energy. *J. Mol. Struct.* **2021**, *1227*, 129369. [CrossRef]

25.	Zaklika, J.; Hładyszowski, J.; Ordon, P.; Komorowski, L. From the Electron Density Gradient to the Quantitative Reactivity Indicators: Local Softness and the Fukui Function. *ACS Omega* **2022**, *7*, 7745–7758. [CrossRef]

26.	Pucci, R.; Angilella, G.G.N. Density functional theory, chemical reactivity, and the Fukui functions. *Found. Chem.* **2022**, *24*, 59–71. [CrossRef]

27.	Nam, W.; Lee, Y.-M.; Fukuzumi, S. Tuning Reactivity and Mechanism in Oxidation Reactions by Mononuclear Nonheme Iron(IV)-Oxo Complexes. *Acc. Chem. Res.* **2014**, *47*, 1146–1154. [CrossRef]

28.	Kal, S.; Que, L. Dioxygen activation by nonheme iron enzymes with the 2-His-1-carboxylate facial triad that generate high-valent oxoiron oxidants. *J. Biol. Inorg. Chem.* **2017**, *22*, 339–365. [CrossRef]

29.	De Visser, S.P.; Mukherjee, G.; Ali, H.S.; Sastri, C.V. Local Charge Distributions, Electric Dipole Moments, and Local Electric Fields Influence Reactivity Patterns and Guide Regioselectivities in α-Ketoglutarate-Dependent Non-heme Iron Dioxygenases. *Acc. Chem. Res.* **2022**, *55*, 65–74. [CrossRef]

30.	Hou, K.; Börgel, J.; Jiang, H.Z.H.; SantaLucia, D.J.; Kwon, H.; Zhuang, H.; Chakarawet, K.; Rohde, R.C.; Taylor, J.W.; Dun, C.; et al. Reactive high-spin iron (IV)-oxo sites through dioxygen activation in a metal–organic framework. *Science* **2023**, *382*, 547–553. [CrossRef] [PubMed]

31.	Ali, H.S.; Henchman, R.H.; de Visser, S.P. Mechanism of Oxidative Ring-Closure as Part of the Hygromycin BiosynthesisStep by a Nonheme Iron Dioxygenase. *ChemCatChem* **2021**, *13*, 3054–3066. [CrossRef]

32.	Goto, M.; Takeshita, M.; Kanda, N.; Sakai, T.; Goedken, V.L. Stoichiometry and Kinetics of Base-Promoted Disproportionation with Concomitant Ligand Oxidation of Tetracyano(l,2-diamine)ferrate(III). *Inorg. Chem.* **1985**, *24*, 582–587. [CrossRef]

33.	Barefield, E.K.; Mocella, M.T. Mechanism of Base Promoted Reduction of Nickel(III) Complexes of Macrocyclic Amines. A Coordinated Ligand Radical Intermediate. *J. Am. Chem. Soc.* **1975**, *97*, 4238–4246. [CrossRef]

34.	Da Costa Ferreira, A.M.; Toma, H.E. Electron-transfer Kinetics and Mechanism of Di-imine Bond Formation in Tetracyano (et hylenediamine) ferrate (II). *J. Chem. Soc. Dalton Trans.* **1983**, *9*, 2051–2055. [CrossRef]

35.	Raleigh, C.J.; Martell, A.E. Oxidative Dehydrogenation of Coordinated l,9-Bis(2-pyridyl)-2,5,8-triazanonane through Formation of a Cobalt Dioxygen Complex intermediate. *Inorg. Chem.* **1985**, *24*, 142–148. [CrossRef]

36.	Morgenstern-Badarau, I.; Lambert, F.; Philippe Renault, J.; Cesario, M.; Maréchal, J.-D.; Maseras, F. Amine conformational change and spin conversion induced by metal-assisted ligand oxidation: From the seven-coordinate iron(II)–TPAA complex to the two oxidized iron(II)–(py)3tren isomers. Characterization, crystal structures, and density functional study. *Inorg. Chim. Acta* **2000**, *297*, 338–350. [CrossRef]

37.	Christian, G.J.; Arbuse, A.; Fontrodon, X.; Angeles Martinez, M.; Llobet, A.; Maseras, F. Oxidative dehydrogenation of an amine group of a macrocyclic ligand in the coordination sphere of a Cu^II complex. *Dalton Trans.* **2009**, *30*, 6013–6020. [CrossRef] [PubMed]

38.	Stubbe, J.A.; van der Donk, W.A. Protein Radicals in Enzyme Catalysis. *Chem. Rev.* **1998**, *98*, 705–762. [CrossRef] [PubMed]

39.	Mandal, A. Radical Chemistry: A Brief History and Overview. *Asian J. Chem.* **2023**, *35*, 1539–1562. [CrossRef]

40.	Zard, S.Z. Recent progress in the generation and use of nitrogen-centred radicals. *Chem. Soc. Rev.* **2008**, *37*, 1603–1618. [CrossRef]

41.	Pratley, C.; Fenner, S.; Murphy, J.A. Nitrogen-Centered Radicals in Functionalization of sp^2 Systems: Generation, Reactivity, and Applications in Synthesis. *Chem. Rev.* **2022**, *122*, 8181–8260. [CrossRef] [PubMed]

42.	Büttner, T.; Geier, J.; Frison, G.; Harmer, J.; Calle, C.; Schweiger, A.; Schönberg, H.; Grützmacher, H. A Stable Aminyl Radical Metal Complex. *Science* **2005**, *307*, 235–238. [CrossRef] [PubMed]

43. Olivos Suarez, A.I.; Lyaskovskyy, V.; Reek, J.N.H.; van der Vlugt, J.I.; de Bruin, B. Complexes with Nitrogen-Centered Radical Ligands: Classification, Spectroscopic Features, Reactivity, and Catalytic Applications. *Angew. Chem. Int. Ed.* **2013**, *52*, 12510–12529. [CrossRef] [PubMed]

44. Kaim, W. Manifestations of Noninnocent Ligand Behavior. *Inorg. Chem.* **2011**, *50*, 9752–9765. [CrossRef]

45. Becke, A.D. Density-functional exchange-energy approximation with correct asymptotic behavior. *Phys. Rev. A* **1988**, *38*, 3098–3100. [CrossRef] [PubMed]

46. Perdew, J.P.; Wang, Y. Accurate and simple analytic representation of the electron-gas correlation energy. *Phys. Rev. B* **1992**, *45*, 13244–13249. [CrossRef]

47. Perdew, J.P.; Burke, K.; Ernzerhof, M. Generalized gradient Approximation Made Simple. *Phys. Rev. Lett.* **1996**, *77*, 3865–3868. [CrossRef]

48. Raghavachari, K.; Trucks, G.W. Highly correlated systems. Excitation energies of first row transition metals Sc–Cu. *J. Chem. Phys.* **1989**, *91*, 1062–1065. [CrossRef]

49. Hehre, W.J.; Ditchfield, R.; Pople, J.A. Self—Consistent Molecular Orbital Methods. XII. Further Extensions of Gaussian—Type Basis Sets for Use in Molecular Orbital Studies of Organic Molecules. *J. Chem. Phys.* **1972**, *56*, 2257–2261. [CrossRef]

50. Frisch, M.J.; People, J.A.; Binkley, J.S. Self-consistent molecular orbital methods 25. Supplementary functions for Gaussian basis sets. *J. Chem. Phys.* **1984**, *80*, 3265–3269. [CrossRef]

51. Liskow, D.H.; Schaefer III, H.F.; Bender, C.F. Geometry and Electronic Structure of the Hydroperoxyl Radical. *J. Am. Chem. Soc.* **1971**, *93*, 6734–6737. [CrossRef]

52. Castro Martínez, F.M.; Páez López, R.D.; Sarmiento Pavía, P.D.; Sosa Torres, M.E.; Kroneck, P.M.H. Cytochrome P450. The Dioxygen-Activating Heme Thiolate. *Met. Ions Life Sci.* **2020**, *20*, 165–197. [CrossRef]

53. Arnold, F.H. Directed Evolution: Bringing New Chemistry to Life. *Angew. Chem. Int. Ed.* **2018**, *57*, 4143–4148. [CrossRef] [PubMed]

54. Neese, F. A perspective on the future of quantum chemical software: The example of the ORCA program package. *Faraday Discuss.* **2024**, *254*, 295–314. [CrossRef] [PubMed]